

## ESTIMATION OF ANEURYSM WALL MOTION FROM 4D COMPUTERIZED TOMOGRAPHIC ANGIOGRAPHY IMAGES

Marcelo A. Castro <sup>a</sup>, María C. Ahumada Olivares <sup>b</sup>, Christopher M. Putman <sup>c</sup>, Juan R. Cebal <sup>d</sup>

<sup>a</sup> *CONICET, Grupo de Investigación y Desarrollo en Bioingeniería, Facultad Regional Buenos Aires, UTN, Medrano 951, Buenos Aires, Argentina, marcelo.a.castro@gmail.com, <http://sites.google.com/site/marceloadriancaastro>*

<sup>b</sup> *Universidad Favaloro, Facultad de Ingeniería, Ciencias Exactas y Naturales, Solís 453, Buenos Aires, Argentina*

<sup>c</sup> *Department of Interventional Neuroradiology, Inova Fairfax Hospital, 3300 Gallows Rd., Falls Church, Virginia, USA*

<sup>d</sup> *Department of Computational and Data Sciences, George Mason University, 4400 University Blvd., Fairfax, Virginia, USA, [jcebral@gmu.edu](mailto:jcebral@gmu.edu), <http://cf.d.gmu.edu/~jcebral>*

**Keywords:** Cerebral aneurysms, Medical image processing, 4D computerized tomographic angiography, Wall motion, Wall shear stress

**Abstract.** It is widely accepted that wall shear stress is associated to aneurysm formation, growth and rupture. Early identification of potential risk factors may contribute to decide the treatment and improve patient care. Previous studies have shown associations between high aneurysm wall shear stress values and both elevated risk of rupture and localization of regions of aneurysm progression. Based on the assumption that damaged regions of the endothelium have different mechanical properties, regions with differentiated wall displacement amplitudes are expected. A previous approach based on the analysis of bidimensional dynamic tomographic angiography images at a limited number of points during the cardiac cycle showed only small displacements in some patients using that simplified and semi-automatic low resolution methodology. The purpose of this work is to overcome some of those limitations. High time and spatial resolution four dimensional computerized tomographic angiography images of cerebral aneurysms were acquired and analyzed in order to identify and characterize wall motion. Images were filtered and segmented at nineteen time points during the cardiac cycle. An average image was computed to generate the vascular model. An unstructured mesh of tetrahedral elements was generated using an advancing front technique. A finite element blood flow simulation was carried out under personalized pulsatile flow conditions. A fuzzy c-means clustering algorithm was used to estimate regions that exhibit wall motion within the aneurysm sac. A good correlation between localization of regions of elevated wall shear stress and regions exhibiting wall motion was found.

## 1 INTRODUCTION

Stroke is the loss of brain function due to disturbances in the blood supply to the brain. This can be due to ischemia (lack of blood flow) caused by blockage (thrombosis or arterial embolism), or hemorrhage (Sims, et al., 2009). Stroke is the leading cause of long-term disability and the third cause of death in the Western World. Subarachnoid hemorrhage is one of the most severe types of stroke, which usually occurs when an intracranial aneurysm ruptures (Hwang, et al., 2007). This kind of aneurysms tends to initiate at or near arterial bifurcations, mostly in the circle of Willis, located at the base of the brain. Although the prevalence of cerebral aneurysm is high (roughly 5%), the yearly risk of subarachnoid hemorrhage for unruptured intracranial aneurysms is low (roughly 1%, for lesions 7 to 10 mm in diameter). However, the consequences are grave: about 50% of mortality, and 50% of morbidity for those who survive. Additionally, treatment of unruptured aneurysms can also be risky. The optimal management of unruptured cerebral aneurysms is controversial and current decision making is mainly based on aneurysm size and location, as derived from the International Study of Unruptured Intracranial Aneurysms (ISUIA) (Wiebers, et al., 2003). Current guidelines suggest that, with rare exceptions, all symptomatic unruptured aneurysms should be treated. On the other hand, incidental aneurysms less than 5mm in diameter should be managed conservatively in virtually all cases, while almost all larger aneurysms should be treated. Exceptions depend on patient age, among other factors (Komotar, et al., 2008). However, it is widely accepted that hemodynamics, particularly the wall shear stress (WSS), plays an important role on the development, growth and rupture of cerebral aneurysms (Castro, 2013a). Previous studies showed that ruptured aneurysms tended to have small impaction zones and complex or unstable flow patterns (Cebal, et al., 2005a). An association between concentrated jets, high WSS and high rupture rate was found in two other studies where cohorts of patients with cerebrovascular networks harboring aneurysms were analyzed using an image-based patient-specific computational fluid dynamics (CFD) methodology in the anterior communicating artery (Castro, et al., 2009a), and a set of terminal aneurysms (Castro, et al., 2009b). That trend was corroborated in a patient population of 210 brain aneurysms at different locations (Cebal, et al., 2011). Other authors analyzed twenty middle cerebral artery aneurysms and also found high WSS values in the group of ruptured aneurysms accompanied with low WSS in their domes, which would suggest that low WSS values may be responsible for aneurysm rupture (Shojima, et al., 2004). However, in that study CFD models were truncated close to the aneurysm neck resulting in a simplified flow lacking of secondary flows. The effect of parent artery on intra aneurysmal hemodynamics was later studied and higher WSS in the aneurysm domes was found to be systematically related to those secondary flows (Castro, et al., 2006a; Castro, et al., 2006b). Another study showed that more than 80% of bleb formation occurs in regions of high WSS (Cebal, et al., 2010). Recently, independent works showed that aneurysms tend to initiate in regions of moderate and elevated WSS (Castro, et al., 2011) and regions of high WSS or high WSS spatial gradient (Kulcsár, et al., 2011). All those findings have encouraged researchers to explore possible connections between hemodynamics, wall motion, wall weakness and aneurysm rupture. Many of the quantitative results of pulsation measurement reported in the literature correspond to experiments with phantoms, simulated images or experimental models (Boechert-Schwartz, et al., 2000; Ueno, et al., 2002, Yaghmai, et al., 2007, Zhang, et al., 2008). A Methodology to estimate wall motion from X-ray dynamic imaging and impose the time-dependent deformation on the vascular CFD models reconstructed from 3D angiographic images was presented (Oubel, et al., 2010). The blood flow characterization obtained from

numerical integration of the Navier-Stokes equations in a rigid wall model did not significantly differ from that in compliant models where the deformation field was extrapolated from the bidimensional measurements (Dempere-Marco, et al., 2006; Castro, et al., 2008). The purpose of this work is to present a methodology to both estimate regions of high wall motion and reconstruct CFD vascular models from 4D computerized tomographic angiography (CTA) data sets.

## 2 METHODS

### 2.1 Angiographic images and vascular modeling

A patient with a cerebral aneurysm in the anterior communicating artery was selected from our data base. A four dimensional computerized tomographic angiography image containing nineteen time points along the cardiac cycle had been acquired using a Philips Integris System (Philips Medical Systems, Best, The Netherlands). Each three dimensional volume consisted of  $512 \times 512 \times 205$  pixels with a spatial resolution of  $0.3125 \times 0.3125 \times 0.6125$  mm covering a field of view of  $16.0 \times 16.0 \times 12.81$  cm. The imaging protocol was approved by the institutional review board and informed consent was obtained from the subject. The data was exported into a PC for mathematic vascular modelling using a previously presented methodology (Yim, et al., 2003; Cebal, et al., 2005a; Castro, et al., 2009b). Images were cropped ( $N_x \times N_y \times N_z$ ) and averaged in order to reduce noise and computational cost. In the inferior regions of the carotid artery masks were applied to all images in order to differentiate the vasculature from extravascular structures, and thus properly reconstruct parent arteries, required for realistic blood flow simulations (Castro, et al., 2006a; Castro, et al., 2006b). Figure 1 shows three axial slices for the first time point. In order to reconstruct the vascular model, a low-noise average image was created. A high-quality volumetric finite element grid composed of roughly 2.5 million tetrahedral elements was generated using an advancing front technique (Löhner, 1996a; Löhner, 1996b; Löhner, 1997) (see Figure 2). Element size was adjusted in order to approximately maintain the same number of elements in both large and small arteries that guarantees the accuracy of the solution.

### 2.2 Blood flow numerical simulations

Finite element blood flow numerical simulations were performed. Blood was modelled as an incompressible fluid with density  $1.0 \text{ g/cm}^3$  and viscosity  $0.04$  Poise. The governing equations were the unsteady Navier-Stokes equations in 3D (Mazumdar, 1992). Vessel walls were assumed rigid, and no slip boundary conditions were applied at the walls. Pulsatile flow conditions derived from phase-contrast magnetic resonance measurement in a healthy subject were imposed at the inlet of the model. Flow waveforms were scaled with the inlet area to achieve a mean WSS of  $15 \text{ dyne/cm}^2$  at the inflows of the model according to a typical mean WSS value, and Murray's and Poiseuille's laws (Sherman, 1981; Cebal, et al., 2008). Fully developed pulsatile velocity profiles were prescribed with use of the Womersley solution (Womersley, 1955; Taylor, et al., 1998). Assuming that all distal vascular beds have similar total resistance to flow, traction-free boundary conditions with the same pressure level were applied at outlet boundaries. Navier-Stokes equations were numerically integrated by using a fully implicit finite-element formulation (Cebal, et al., 2005b). Our methodology is based on a projection scheme which arises from the hyperbolic character of the advection operator and the elliptic character of the pressure-Poisson equation. A fully implicit finite element formulation that yields to stable solutions for arbitrary time steps was utilized. The discretized

momentum equation is solved using a generalized minimal residual (GMRES) algorithm, while the pressure equation, which is obtained by taking the divergence of the momentum and considering the incompressibility constraint, is solved using an incomplete lower-upper (ILU) preconditioned conjugate gradient solver. The algorithm is iterated until convergence is achieved at each time step. Two cardiac cycles using 100 time-steps per cycle were computed, and all of the results reported correspond to the second cardiac cycle.

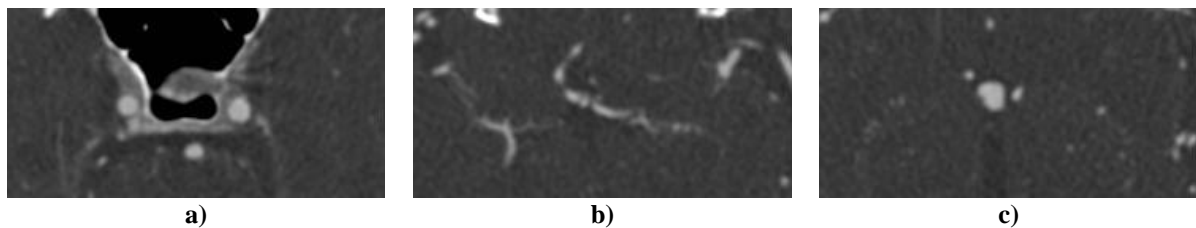


Figure 1: Axial slices for the first time point. The following vascular structures are shown: a) both internal carotid arteries (largest and brightest spots) along with the basilar artery (smaller spot); b) both A1 segments of the anterior cerebral arteries, the anterior communicating artery and the inferior part of the aneurysm (at the center of the image); c) both A2 segments of the anterior cerebral arteries along with the superior part of the aneurysm (at the center of the image). See Figure 2 for A1 and A2 segments.

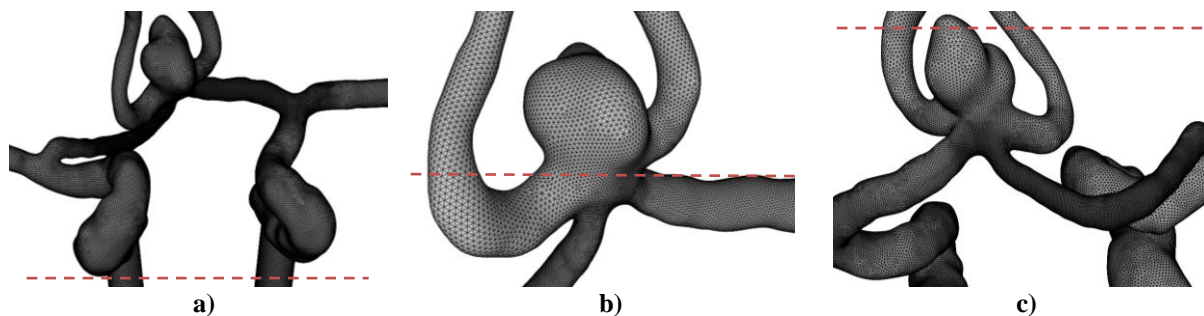


Figure 2: a) Vascular model containing both internal carotid arteries, anterior cerebral arteries and middle cerebral arteries; b) Grid of triangles (anterior view); c) Grid of triangles (posterior view). Red dotted lines indicate the location of the axial slices displayed in Figure 1. The aneurysm is located at the anterior communicating artery, which has two afferent arteries (the A1 segments of both anterior cerebral arteries), and two efferent arteries (the A2 segments of both anterior cerebral arteries).

### 2.3 Fuzzy c-means algorithm for wall motion estimation

In order to detect the regions where wall motion is not negligible, images were segmented in different clusters, and the time evolution of segmented clusters at every slice within the volume of interest was analysed. For each of the  $N=19$  three dimensional images ( $N_x \times N_y \times N_z$ ) the same selected number of  $NS$  slices covering the whole aneurysm was taken for the analysis. A set of  $NS$  images  $N_x \times N_y \times N$  was created to analyse the time evolution of pixel intensities in all  $NS$  slices. Four classes were identified with intensities well differentiated, two of which corresponded to the background ( $C1$  and  $C2$ ), and the other two are associated to the border of the vascular domain ( $C3$ ) and the vasculature itself ( $C4$ ). A four-class fuzzy c-means algorithm was utilized to create the four images corresponding to the membership value  $W$  ( $0 < W < 1$ ) in each of the  $NS$  images, which estimates the probability of each pixel to belong to the corresponding class. Particularly, for the image associated to  $C4$ , the pixel intensity is an estimation of the probability of that pixel to belong to the vasculature.

The fuzzy c-means algorithm minimizes the cost function  $J$  over all pixels  $NP=N_x*N_y$ , and all classes  $K$ , for each slice (1)

$$J = \sum_{j=1}^{NP} \sum_{c=1}^K (W_{cj})^q \|M_c - I_j\|^2 \quad (1)$$

where  $M_c$  is the centroid of class  $c$ ,  $I_j$  is the intensity of pixel  $j$ ,  $W_{cj}$  is the corresponding membership value at pixel  $j$  for class  $c$ , and  $q$  is the weighting exponent on each membership value, which determines the amount of fuzziness of the resulting segmentation. The centroids for each class are given by (2).

$$M_c = \frac{\sum_{j=1}^{NP} (W_{cj})^q I_j}{\sum_{j=1}^{NP} (W_{cj})^q} \quad (2)$$

The membership values, which are defined by (3), must meet the normalization constraint given by (4),

$$W_{cj} = \frac{A}{\|M_c - I_j\|^{\frac{2}{q-1}}} \quad (3)$$

$$\sum_{c=1}^K W_{cj} = 1 ; \forall j \in Im \quad (4)$$

where  $Im$  is the image, and the normalization constant  $A$  in (3) can be computed using (4), resulting in the following expression for the membership values (5).

$$W_{cj} = \frac{\|M_c - I_j\|^{-\frac{2}{q-1}}}{\sum_{d=1}^K \|M_d - I_j\|^{-\frac{2}{q-1}}} \quad (5)$$

Assuming a weighting exponent  $q=2$ , the final expression for the membership values and the centroids of each class are given by (7) and (8), respectively. For single spectral analysis, the norm in equation (7) is equivalent to the absolute value of the difference between the given centroid and current pixel intensity.

$$W_{cj} = \frac{\|M_c - I_j\|^{-2}}{\sum_{d=1}^K \|M_d - I_j\|^{-2}} \quad (7)$$

$$M_c = \frac{\sum_{j=1}^{NP} (W_{cj})^2 I_j}{\sum_{j=1}^{NP} (W_{cj})^2} \quad (8)$$

Minimization is achieved by an iterative process that performs two computations. First, the minimization process computes the membership functions using the current estimate of the centroids. Note that centroids are initialized at the beginning by equally dividing the

sample in the given number of classes. Afterwards, the minimization process computes the centroids using the current estimates of the membership functions (Chuang, et al., 2006).

It is expected that membership values should significantly change in time for pixels close to a moving boundary. In order to characterize that change, the maximum difference along the  $N$  time slices was computed for each of the  $N_x \times N_y$  pixels and for each of the  $NS$  images. This information was used to reconstruct a  $N_x \times N_y \times NS$  image where the pixel intensity represents the maximum difference in time of the membership value of class  $C4$ . Since  $C1$  and  $C2$  clusters correspond to the lowest intensities and  $C4$  to the highest ones, pixels that change from vasculature to background due to wall motion are expected to have significant different membership values for class  $C4$ . That change is used as an estimation of the probability of those pixels to experiment a wall motion. That image was segmented using different thresholds.

## 2.4 Wall shear stress analysis

Maps of WSS magnitude were created to visualize the distribution of shear forces on the aneurysm wall at the systolic peak where the maximum values are expected. Regions that are likely to change from vasculature to background (Section 2.3) were isolated and compared to the shear stress distribution over the wall. Although in this preliminary study the model walls were rigid, it is expected that flow patterns should remain roughly unchanged for moderate wall displacements (Dempere-Marco, et al., 2006; Oubel, et al., 2010). This hypothesis will be further tested in large aneurysms with high deformations using dynamic tomographic angiography images. Streamlines were created and the velocity field was imaged in order to investigate the relation between the localisation of the impaction zone, the maximum wall motion and the elevated WSS values, and the flow characterization.

## 3 RESULTS

Figure 3a corresponds to a selected axial slice and a given time were the brightest spots correspond to both A2 segments of the anterior cerebral arteries (upper left corner) and the superior part of the anterior communicating artery aneurysm (brightest and largest spot). Visual inspection of that image revealed a background (extravascular structures) with a large range of pixel intensities, while the highest intensities corresponded to the vasculature. A transition takes place in the boundary between the vasculature and the background. Figures 3b through 3e correspond to membership values for classes  $C1$  through  $C4$ , respectively. Darker regions in the image for class  $C_i$  ( $i=1,2,3,4$ ), correspond to pixels that unlikely belong to that particular class.

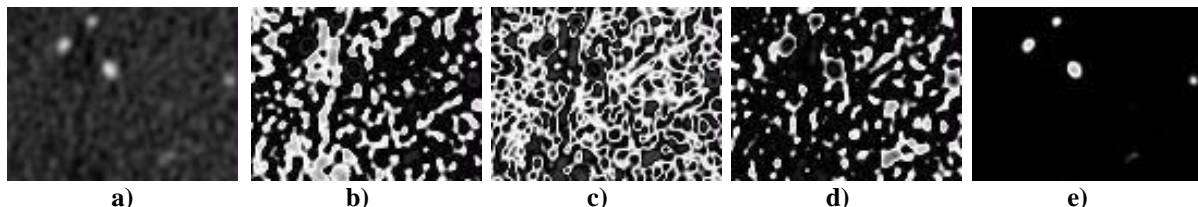


Figure 3: a) Selected axial slice at a given time; b) Membership values for class  $C1$ ; c) Membership values for class  $C2$ ; d) Membership values for class  $C3$ ; e) Membership values for class  $C4$ .

Slightly localised changes in the aneurysm morphology along the cardiac cycle were observed. The difference between  $C4$  images at different times was computed. Changes due to noise are not extremely high and are observed in small disconnected regions. On the other

hand, changes due to wall motion are associated to higher values and are observed in larger areas. An intensity-based segmentation for different thresholds ( $T1=0.325$  and  $T2=0.400$ ) was performed in order to investigate the location where the highest displacements take place. The WSS distribution at the systolic peak is displayed in Figure 4a. The segmented pixels are shown along with the WSS distribution at the systolic peak (Figure 4b and 4c, for  $T1$  and  $T2$ , respectively). The grey regions in those images correspond to pixels that experiment a change in the membership value for class  $C4$  higher than  $T1$  and  $T2$ , respectively, displayed over the WSS distribution. As it was expected, the lower the threshold, the larger the segmented region. For example, in Figure 4c, if any of the grey pixels belongs to class  $C4$  with a membership value of 0.80 at a given time, there exists another time when that value drops below 0.40.

Streamlines were computed in order to study whether or not the aneurysm behaves as a bilateral aneurysm (e.g., it receives blood from two differences sources), and to investigate the dependence of the WSS on the flow pattern. Blue streamlines are originated in the right internal carotid artery, and red ones do it in the left carotid artery (see Figure 5c). Complex velocity field observed in Figures 5b and 5c is due to the collision of both jets. However, intraaneurysmal flow pattern is dominated by the left inflow. The impaction zone is located at the peak of the WSS distribution, and close to where the wall motion is observed, and where both jets collide (Figure 5a). The WSS averaged within the impaction zone at the systolic peak was as high as  $69.2 \text{ dyn/cm}^2$ , while in the opposite low WSS region it was  $0.51 \text{ dyn/cm}^2$ .

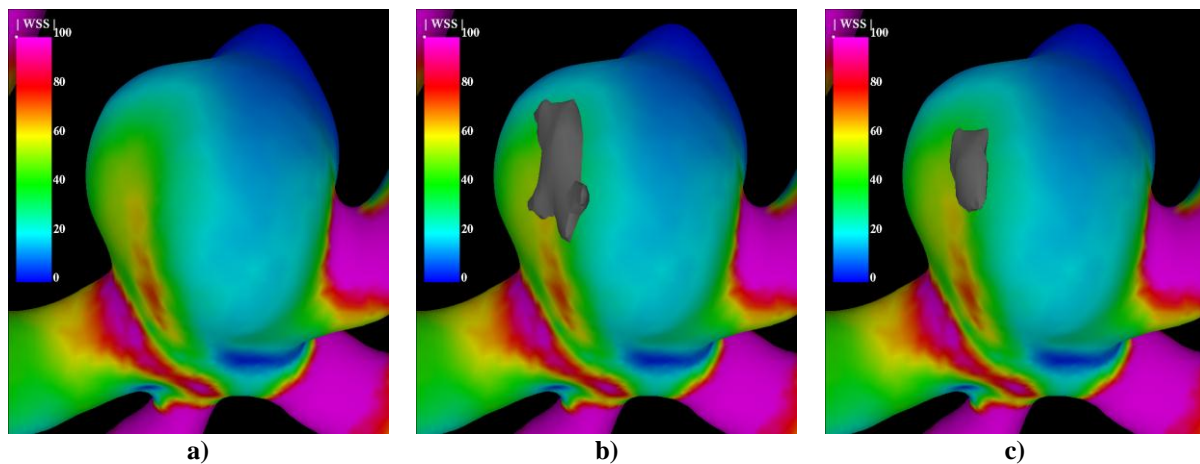


Figure 4: WSS distribution at the systolic peak (a). WSS distribution at the systolic peak along with the segmented region where higher wall displacements are expected for  $T1=0.325$  (b) and  $T2=0.400$  (c).

#### 4 DISCUSION

The purpose of this work was to design and test a methodology to estimate both the aneurysm wall shear stress, and aneurysm wall motion from 4D computerized tomographic angiography images. A test case was randomly selected from our data base. The patient had a large aneurysm in the anterior communicating artery. Acquired data consisted of nineteen high resolution three dimensional images along the cardiac cycle. Images were averaged to reduce the impact of noise on the reconstruction of the vascular model used to generate the finite element unstructured volumetric grid for the blood flow simulation and wall shear stress estimation. In order to estimate the localization of regions that exhibit an important wall displacement, the time evolution of individual slices across the aneurysm was analysed and a fuzzy c-means clustering algorithm was applied to simultaneously segment all time points in

four different classes for each slice. Four classes were identified. The membership values for each class were recorded. Pixels within the vascular domain but close to a moving boundary exhibited a change in those values. That difference was segmented using two different thresholds. The regions exhibiting important displacements were overlapped with the WSS distribution. Maximum WSS values at the systolic peak occurred close to the region where noticeable displacements took place. Particularly, this anterior communicating artery aneurysm behaved as a bilateral aneurysm, which means that received blood from both A1 segments of the anterior cerebral arteries (Castro, et al., 2009a), and high wall motion occurred close to where both jets collided. This strategy estimates the wall motion from a 3D analysis and overcomes some of the limitations from a previous methodology where the motion was measured in a plane and extrapolated to the aneurysm (Oubel, et al., 2010).

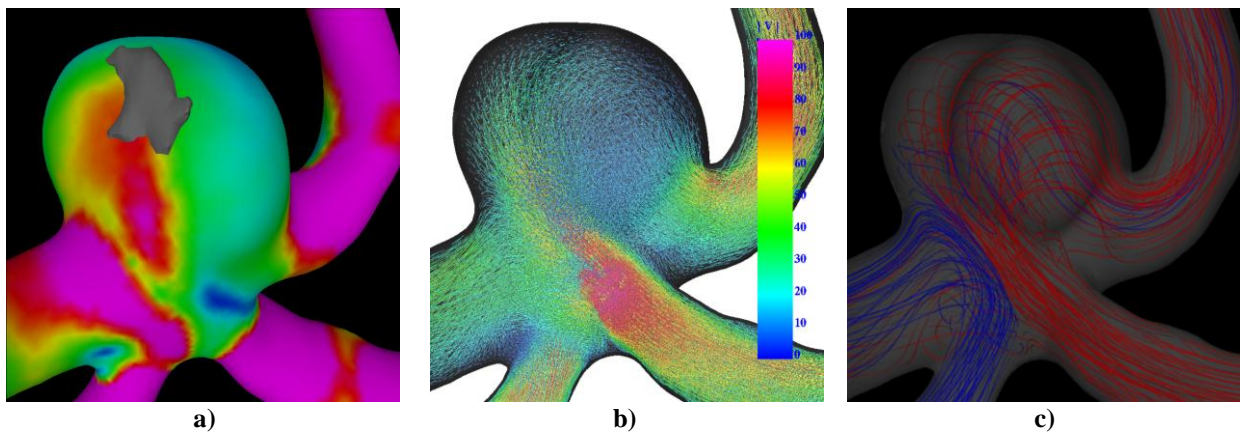


Figure 5: a) WSS distribution at the systolic peak along with the segmented region where higher wall displacements are expected ( $TI=0.325$ ); b) Velocity field; c) Streamlines colored according to the source of inflow. Blue streamlines are originated at the right internal carotid artery, and red to the left internal carotid artery.

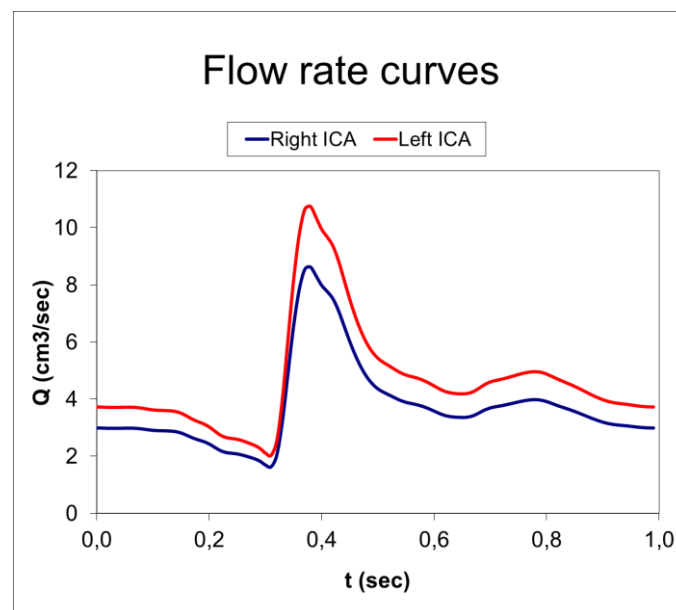


Figure 6: Flow rate waveforms imposed at the Right Internal Carotid Artery (blue) and Left Internal Carotid Artery (red) of the vascular model at 60 bpm. Lower flow rates correspond to smaller cross sectional areas, according to Murray's Law.

The methodology has some limitations. First, the computational fluid dynamics simulation was performed under the assumption of rigid walls. Although this assumption is not accurate, it was observed in a previous work that moderate wall displacements along the cardiac cycle do not significantly change the WSS distribution over the wall of the aneurysm sac (Dempere-Marco, et al., 2006; Castro, et al., 2008). However, in future works wall motion will be also included in CFD blood flow simulations. Second, bilateral anterior communicating artery aneurysms have flow patterns that may depend on inflow conditions. We imposed the same waveform at both internal carotid arteries, but scaled according to their cross-sectional areas based on a typical wall shear stress value, and both Murray's and Poiseuille's laws (Figure 6). It was previously observed that differences in either those mean flow rates at the inflow segments or waveform phases may slightly relocate the region where the maximum wall shear stress appeared. However, the impact region is always located where the individual jets impact the aneurysm in the hemodynamic unilateral cases. Therefore, in this case slightly relocated may be expected. It is also worth mentioning that numerical solution strongly depend on the geometry (Cebral et al., 2005b), therefore accurate reconstructions of the aneurysm sac and parent arteries are required for clinical applicability (Castro et al., 2006a; Castro et al., 2006b). Other parameters and assumptions like blood rheology (Castro et al., 2013b), distal flow division, and inclusion of smaller arteries in the model, do not affect the hemodynamic characterization, like impaction zone, WSS distribution, jet concentration, etc., whose association with initiation, growth and rupture are sought (Cebral et al., 2005b). In previous works the methodology was evaluated and validated by means analytical solutions, *in vivo* and *in vitro* measurements (Cebral et al., 2007; Castro et al., 2008; Cebral et al., 2009; Castro, 2013a). From those studies a typical number of elements in a cross sectional area to achieve accuracy and mesh independence was determined and used to automatically decrease element size in small arteries and thus keep the number of elements in an arterial cross sectional area roughly constant (Castro et al., 2008). Finally, in order to estimate the probability to belong to a given class, images were not pre-processed. Consequently, pixels in the background that changed from one class to another due to the noise were also detected as possible candidates. However, those regions were isolated and the change in the probability was not as large as that observed in boundary pixels. It was observed that higher thresholds kept the large regions where displacements occurred due to wall motion, and discarded those small regions due to the noise.

## CONCLUSIONS

The present work shows that dynamic computerized tomographic angiography images can be used to estimate the location of regions with both aneurysm wall motion and high wall shear stress by means of a combination of image segmentation algorithms and image-based computational fluid dynamics blood flow simulations. The results suggest that aneurysm wall tends to exhibit higher displacements along the cardiac cycle in regions with elevated wall shear stress and complex flow pattern. Further analysis will be carried out to corroborate this trend.

## ACKNOWLEDGEMENTS

Marcelo Castro wants to acknowledge CONICET (Consejo Nacional de Investigaciones Científicas y Técnicas), MINCyT (Ministerio de Ciencia y Tecnología – Project PICT Bicentenario # 984), UTN (Universidad Tecnológica Nacional, Project PID # 1579), and Fundación Florencio Fiorini, Buenos Aires, Argentina, for financial support.

## REFERENCES

- Boecher-Schwarz, H.G., Ringel, K., Kopacz, L., Heimann, A., Kempfski, O., Ex vivo study of the physical effect of coils on pressure and flow dynamics in experimental aneurysms. *Am J Neuroradiol*, 21:1532–1536, 2000.
- Castro, M.A., Putman, C.M., Cebal, J.R., Effects of Parent Vessel Geometry on Intraaneurysmal Flow Pattern. *Proc. SPIE Medical Imaging 2006: Physics of Medical Imaging Image Reconstruction*, 6143:123–131, 2006a.
- Castro, M.A., Putman, C.M., Cebal, J.R., Computational fluid dynamics modeling of intracranial aneurysms: effects of parent artery segmentation on intra-aneurysmal hemodynamics. *Am J Neuroradiol*, 27:1703–1709, 2006b.
- Castro, M.A., Putman, C.M., Cebal, J.R., Computational hemodynamics of cerebral aneurysms: Assessing the risk of rupture. *VDM Verlag*, 2008.
- Castro, M.A., Putman, C.M., Cebal, J.R., Hemodynamic Patterns of Anterior Communicating Artery Aneurysms: A Possible Association with Rupture. *Am J Neuroradiol*, 30(2):297–302, 2009a.
- Castro, M.A., Putman, C.M., Radaelli, A., Frangi, A.F., Cebal, J.R., Hemodynamics and rupture of terminal cerebral aneurysms. *Acad Radiol*, 16(19):1201–1207, 2009b.
- Castro, M.A., Putman, C.M., Cebal, J.R., Computational analysis of anterior communicating artery aneurysm shear stress before and after aneurysm formation. *Journal of Physics C.S.*, 32:1–7, 2011.
- Castro, M.A., Understanding the role of hemodynamics in the initiation, progression, rupture, and treatment outcome of cerebral aneurysm from medical image-based computational studies, *ISRN Radiology*, 2013:1–17, 2013a.
- Castro, M.A., Ahumada Olivares, M.C., Putman, C.M., Cebal, J.R., Wall motion an hemodynamics in intracranial aneurysms, *Journal of Physics C.S.*, 1-9, 2013
- Cebal, J.R., Castro, M.A., Burgess, J.E., Pergolizi, R.S., Sheridan, M.J., Putman, C.M., Characterization of cerebral aneurysm for assessing risk of rupture using patient-specific computational hemodynamics models. *Am J Neuroradiol*, 26:2550–2559, 2005a.
- Cebal, J.R., Castro, M.A., Appanaboyina, S., Putman, C., Millán, D., Frangi, A., Efficient Pipeline for Image-Based Patient-Specific Analysis of Cerebral Aneurysms Hemodynamics: Technique and Sensitivity. *IEEE - Trans Med Imag - Special Issue on Vascular Imaging*, 24(4):457–467, 2005b.
- Cebal, J.R., Pergolizzi, R.S., Putman, C.M., Computational Fluid Dynamics Modeling of Intracranial Aneurysms: Qualitative Comparison with Cerebral Angiography, *Academic Radiology*, 14: 804–813, 2007.
- Cebal, J.R., Castro, M.A., Putman, C.M., Alperin, N., Flow-area relationship in internal carotid and vertebral arteries. *Physiol Meas*, 29(10):585–594, 2008.
- Cebal JR, Putman CM, Alley MT, Hope T, Bammer R, Calamante F, Hemodynamics in Normal Cerebral Arteries: Qualitative Comparison of 4D Phase-Contrast Magnetic Resonance and Image-Based Computational Fluid Dynamics, *Journal of Engineering Mathematics*, 64(4): 367–378, 2009.
- Cebal, J.R., Sheridan, M.J., Putman, C.M., Hemodynamics and Bleb Formation in Intracranial Aneurysms. *Am J Neuroradiol*, 31:304–310, 2010.
- Cebal, J.R., Mut, F., Weir, J., Putman, C.M., Association of hemodynamic characteristics and cerebral aneurysm rupture. *Am J Neuroradiol*, 32:264–270, 2011.
- Chuang, K.-S., Tzeng, H.-L., Chen, S., Wu, J., Chen, T.-J., Fuzzy c-means clustering with spatial information for image segmentation. *Comput Medl Imag and Graph*, 30:9–15, 2006.
- Dempere-Marco, L., Oubel, E., Castro, M.A., Putman, C.M., Frangi, A.F., Cebal, J.R., Estimation of wall motion in intracranial aneurysms and its effects on hemodynamic patterns. *Lecture Notes in Computer Science*, 4191:438–445, 2006.
- Hwang, S., Kim, K., Nam, T., A pseudoaneurysm appeared after rebleeding. *Journal of Korean Neurosurgical Society*, 41:134–136, 2007.

- Komotar, R.J., Mocco, J., Solomon, R.A., Guidelines for the surgical treatment of unruptured intracranial aneurysms: the first annual J. Lawrence pool memorial research symposium—controversies in the management of cerebral aneurysms. *Neurosurgery*, 62(1):183–193, 2008.
- Kulcsár, Z., Ugron, A., Marosfo, M., Berentei, Z., Paal, G., Szikora, I., Hemodynamics of Cerebral Aneurysm Initiation: The Role of Wall Shear Stress and Spatial Wall Shear Stress Gradient. *Am J Neuroradiol*, 32(3):587–594, 2011.
- Löhner, R., Extensions and improvements of the advancing front grid generation technique, *Comp Meth App Mech Eng*, 5:119–132, 1996a.
- Löhner, R., Regridding surface triangulations. *J Comput Phys*, 126:1–10, 1996b.
- Löhner, R., Automatic unstructured grid generators, *Finite Elements Analysis Design*, 25:111–134, 1997.
- Mazumdar, J.N., Biofluid Mechanics. *World Scientific*, Singapore, 1992.
- Oubel, E., Cebal, J.R., De Craene, M., Blanc, R., Blasco, R., Macho, J., Putman, C.M., Frangi, A.F., Wall motion setimation in Intracranial aneurysms. *Physiol Meas*, 31:1119–1135, 2010.
- Sherman, T.F., On connecting large vessels to small. The meaning of Murray's law. *J Gen Physiol*, 78:431–453, 1981.
- Shojima, M., Oshima, M., Takagi, K., Torii, R., Hayakawa, M., Katada, K., Morita, A., Kirino, T.. Magnitude and role of wall shear stress on cerebral aneurysm: computational fluid dynamic study of 20 middle cerebral artery aneurysms. *Stroke*, 35:2500–2505, 2004.
- Sims, N.R., Muyderman, H., Mitochondria, oxidative metabolism and cell death in stroke. *Biochimica et Biophysica Acta*, 1802(1):80–91, 2009.
- Taylor, C.A., Hughes, T.J.R., Zarins, C.K., Finite element modeling of blood flow in arteries. *Comp Meth Appl Mech Engin*, 158:155–196, 1998.
- Ueno, J., Matsuo, T., Sugiyama, K., Okeda, R., Mechanism underlying the prevention of aneurismal rupture by coil embolization. *J Med Dental Sci*, 49:135–141, 2002.
- Wiebers, D.O., et al., International study of unruptured intracranial aneurysms investigators. Unruptured intra-cranial aneurysms: natural history, clinical outcome, and risks of surgical and endovascular treatment. *Lancet*, 362:103–110, 2003.
- Womersley, J.R., Method for the calculation of velocity, rate of flow and viscous drag in arteries when the pressure gradient is known. *J Physiol*, 127:553–563, 1955.
- Yaghmai, V., Rohany, M., Shaibani, A., Huber, M., Soud, H., Russell, E.J., Walker, M.T., Pulsatility imaging of saccular aneurysm model by 64-slice CT with dynamic multiscan technique. *J Vasc Intervent Radiol*, 18:785–788, 2007.
- Yim, P., Vasbinder, G.B., Ho, V.B., Choyke, P.L., Isosurfaces as deformable models for magnetic resonance angiography. *IEEE – Trans Med Imag*, 22(7):875–881, 2003.
- Zhang, C., Villa Uriol, M.C., De Craene, M., Pozo, J.M., Frangi, A.F., Time-resolved 3D rotational angio-graphy reconstruction: Towards cerebral aneurysm pulsatile analysis. *Int J Comput Assist Radiol Surg*, 3:S44–46, 2008.